Near-native state imaging by cryo-soft-X-ray tomography reveals remodelling of cytoplasmic vesicles and mitochondria during HSV-1 infection

Kamal L. Nahas[1,2], Viv Connor[1], Maria Harkiolaki[2]*, Colin M. Crump[1]*, Stephen C. Graham[1]*

[1]Department of Pathology, University of Cambridge, Tennis Court Road, Cambridge CB2 1QP, United Kingdom.

[2] Beamline B24, Diamond Light Source, Harwell Science and Innovation Campus, Didcot OX11 0DE, United Kingdom.

*Corresponding authors: Maria Harkiolaki, maria.harkiolaki@diamond.ac.uk; Colin M. Crump, cmc56@cam.ac.uk; Stephen C. Graham, scg34@cam.ac.uk

ORCIDs: KLN 0000-0003-3501-8473; CMC 0000-0001-9918-9998; SCG 0000-0003-4547-4034; MH 0000-0001-8091-9057

Contributions: Conceptualization: MH, CMC, SCG; Data Curation: KLN; Funding Acquisition: MH, CMC, SCG; Investigation: KLN, VC, CMC, SCG; Project Administration: MH, CMC, SCG; Resources: MH; Software: KLN; Supervision: MH, CMC, SCG; Visualization: KLN; Writing – Original Draft Preparation: KLN, CMC, SCG; Writing – Review & Editing: KLN, MH, CMC, SCG

Short Title: Cryo-soft-X-ray tomography of HSV-1 infection

Keywords: Herpesvirus, virus:host interactions, cryoSXT

Abstract

Herpes simplex virus-1 (HSV-1) is a large, enveloped DNA virus and its assembly in the cell is a complex multi-step process during which viral particles interact with numerous cellular compartments such as the nucleus and organelles of the secretory pathway. Transmission electron microscopy and fluorescence microscopy are commonly used to study HSV-1 infection. However, 2D imaging limits our understanding of the 3D geometric changes to cellular compartments that accompany infection and sample processing can introduce morphological artefacts that complicate interpretation. In this study, we used a 3D imaging technique (soft X-ray tomography) to observe differences in whole-cell architecture between HSV-1 infected and uninfected cells. To protect the near-native structure of cellular compartments, we used a non-disruptive sample preparation technique involving rapid cryopreservation. We observed viral capsids and assembly intermediates interacting with nuclear and cytoplasmic membranes. Furthermore, we observed differences in the morphology of specific organelles between uninfected and infected cells. The local concentration of cytoplasmic vesicles at the juxtanuclear compartment increased and their mean width decreased as infection proceeded. Furthermore, mitochondria in infected cells were elongated and highly branched, suggesting that altered dynamics of mitochondrial fission/fusion accompany HSV-1 infection. Our results demonstrate that high-resolution 3D images of cellular compartments can be captured in a near-native state using soft X-ray tomography and have revealed that infection causes striking changes to the morphology of intracellular organelles.

41 **Importance**

42 Ultrastructural changes to the morphology and organization of cellular compartments during herpes
43 simplex virus-1 (HSV-1) infection have not been studied under near-physiological conditions. In this
44 study, near-native state X-ray imaging was used to image the ultrastructure of HSV-1 and cellular
45 compartments during infection, identifying striking changes to the abundance and organization of
46 cytoplasmic vesicles and mitochondria. The concentration of vesicles in the juxtanuclear region
47 increased with time post infection, which could represent an increasing supply of vesicles to support
48 capsid envelopment. Mitochondria are dynamic cellular compartments that undergo fusion to share
49 resources and fission followed by mitophagy to recycle damaged components. Here we show that
50 mitochondria tend to elongate and form highly-branched networks as infection progresses, suggesting
51 fusion predominates over fission during HSV-1 infection. These findings offer insight into stages of virion
52 morphogenesis and the cellular response to infection.

53

54

Introduction

Herpes simplex virus-1 (HSV-1) is a large, enveloped DNA virus in the *Alphaherpesvirinae* subfamily of *Herpesviridae* that establishes a persistent life-long latent infection in sensory and sympathetic neurons, occasionally reactivating to cause lytic replication in oral or genital mucosal epithelial cells that culminates in cold sores and genital herpes, respectively[1]. The production of viral particles during lytic replication is a complex process involving multiple cellular compartments[2–6].

In the first step of virion morphogenesis, capsid assembly and genome packaging occur in the nucleus[7]. Fully formed nucleocapsids must cross the nuclear envelope to migrate into the cytoplasm and undergo latter stages of virus assembly – a process which involves close interaction between nucleocapsids and the membranes of the nuclear envelope. Unlike individual proteins, the nucleocapsids are too large to pass through nuclear pores and must therefore first bud into the perinuclear space through the inner-nuclear membrane, forming a perinuclear viral particle (primary envelopment). The envelope of this particle subsequently fuses with the outer-nuclear membrane to release the nucleocapsid into the cytoplasm (de-envelopment)[8–11]. Numerous copies of multiple (≥ 23) viral proteins deposit on the surface of nucleocapsids in the nucleus and cytoplasm to form an amorphous proteinaceous layer known as the tegument[12]. Tegument proteins have multiple important roles during infection, including the promotion of virion maturation[2,3,6]. Several cytoplasmic compartments are essential to virion morphogenesis: viral proteins are synthesized and modified in the endoplasmic reticulum and Golgi complex and, in a process known as secondary envelopment, nucleocapsids acquire their membrane envelope from cytoplasmic vesicles that are thought to be derived from the *trans*-Golgi network and the endosomal system[2,3,13]. In addition to compartments directly involved in virion assembly, the cytoskeleton and other cellular organelles, such as mitochondria and lysosomes, can become remodelled in response to infection[14–16]. Understanding how the morphology and organization of cellular compartments change during infection could illuminate their involvement in virion morphogenesis and in the cellular response to HSV-1 infection.

Previous studies to characterize remodelling of cellular compartments have identified numerous changes that accompany HSV-1 infection, including the fragmentation of the Golgi complex and the condensation of the endoplasmic reticulum around the nuclear rim[17,18]. A more comprehensive study has recently been carried out using a recombinant form of HSV-1, known as the “timestamp” reporter

virus, expressing fluorescent chimeras of the early protein ICP0 and the late protein gC to distinguish between early and late stages of infection[16]. Eight cellular compartments were compared between uninfected and timestamp virus-infected human TERT-immortalized human foreskin fibroblast (HFF-hTERT) cells, with high-resolution spatial data collected using structured illumination microscopy (SIM) and expansion microscopy. Numerous changes in the morphology of cellular compartments were observed as infection progressed, such as fragmentation of the Golgi complex at late stages of infection, concentration of endosomes and lysosomes at a juxtanuclear compartment, and elongation of mitochondria[16]. However, the extent to which sample preparation strategies may damage the morphology of cellular structures remains poorly understood and it is possible that disruptive techniques such as immunostaining or sample expansion could introduce artefacts in cellular ultrastructure[19–21]. Moreover, it is not clear if these changes to cellular compartments are consistent across different cell types used to study HSV-1 infection.

In this study, we investigated changes to cellular compartments during infection with the HSV-1 timestamp reporter virus using soft X-ray tomography of cryopreserved samples (cryoSXT). Soft X-rays used for this analysis have a lower energy (~500 eV)[22] and longer wavelength than the “hard” X rays typically used for medical imaging (~15-30 keV)[23] or X-ray crystallography (~6–20 keV)[24]. The wavelengths of soft X-rays used for cryoSXT are in the “water window” where structured carbon-rich structures in the cell such as membranes produce considerable contrast whereas oxygen-rich structures such as the “watery” cytosol remain transparent, thereby enabling cellular compartments to be observed[22]. We used this label-free technique to image the ultrastructure of infected (and control) cells, monitoring the 3D geometry and organization of cellular compartments[25]. The ultrastructure of the samples was protected in a near-native state using a non-disruptive cryopreservation protocol[26]. Our study focused on the ultrastructural changes that accompany HSV-1 infection of human osteosarcoma U2OS cells, allowing comparison with previous reports from infection of HFF-hTERT cells[16]. Although a few differences were observed between the extent of Golgi fragmentation and the subcellular distribution of ICP0, we determined that remodelling of cytoplasmic vesicles and mitochondria was largely similar between these cultured cells. Furthermore, the high resolution afforded by cryoSXT revealed that mitochondria become highly branched during HSV-1 infection.

Results

HSV-1 viral particles and assembly intermediates are detectable by cryoSXT

While cryoSXT has been used to image virus particles in infected cells[25,27], it was unclear whether 'naked' HSV-1 capsids, which are approximately 125 nm in diameter[28,29], would be large enough and offer sufficient contrast to be observed with this imaging method. To establish a baseline, we grew uninfected HFF-hTERT cells on holey-carbon electron microscopy (EM) grids and plunge cryocooled them for imaging by cryoSXT. Unlike a glass lens that focuses light by refraction, a zone plate was used to focus the X rays by diffraction: a zone plate is a diffraction grating composed of a series of concentric rings in which alternating rings are transparent to X rays and the resolution is determined by the diameter of the outermost ring[30]. 25 nm zone plates, affording up to 30 nm resolution, were used for our experiments here. To produce a tomogram, a series of X-ray projection images were collected from a single 9.46×9.46 μm field of view in the cell, with each projection collected following rotation of the specimen around an axis normal to the incident X-ray beam (tilt series). For each tomogram the projections spanned up to 120° of rotation with increments of 0.2° or 0.5° per image. To correct for vibrations in the microscope during imaging, the projections in the series were aligned together in the program IMOD[31] using gold fiducials or lipid droplets as landmarks for registration. We collected 19 tilt series that were processed into 3D tomograms and we found that the content of nuclei in uninfected cells appear relatively featureless (**Fig 1A**).

Given that the nucleus is the site of capsid assembly, we sought to determine whether an abundance of capsids could be detected in infected cells. To this end, HFF-hTERT cells were cultured on holey-carbon EM grids, infected with 2 plaque-forming units (PFU) per cell of HSV-1 and plunge frozen at 16 hours post-infection (hpi). Infected cells were imaged via cryoSXT using a 40 nm zone plate objective (**Fig. 1B**), illuminating a 15.14×15.14 μm field of view, using the image acquisition and analysis workflow detailed above. These samples were prepared and cryopreserved on three different occasions and 98 tomograms were collected in total. Numerous dark puncta were observed in the nucleus of infected cells (**Fig. 1C**). We interpreted these puncta to be HSV-1 capsids because capsids are rich in carbon and phosphorous, being proteinaceous shells surrounding tightly packed DNA genomes, and these elements exhibit strong absorption at the 500 eV X-ray energy used here for imaging[22]. During virus assembly, capsids enter the perinuclear space by budding at the inner nuclear membrane (primary

envelopment), forming a membrane-wrapped perinuclear viral particle that rapidly fuses with the outer nuclear membrane *en route* to the cytoplasm[9]. These enveloped virions in the perinuclear space are infrequently observed by EM because they are short-lived and the thin sectioning required for imaging using electron light decreases the probability that such structures will be present within the cellular volume being examined. The high penetrating power of soft X-rays in unstained cryopreserved samples (> 10 μm) removes the requirement for sectioning, allowing the entire depth of the cell to be imaged simultaneously for any given field of view. This increases the likelihood of observing short-lived structures such as primary enveloped viral particles. Dark puncta within the nuclear envelope that are likely to be perinuclear viral particles were found 11 times in 98 tomograms (**Fig. 1D**). The perinuclear viral particles appear to expand the perinuclear space and distend the nuclear envelope, as shown in a segmented image (**Fig. 1E**). The width of the nuclear envelope at putative sites of primary envelopment (190.6 ± 6.01 nm SEM; N=11) is significantly greater than the width of the nuclear envelope in other places on the same tomograms (99.8 ± 3.57 nm SEM; N=11; paired t-test p-value=1.93×10^{-9}) (**Fig. 1F**). This demonstrates the substantial deformation of the nuclear envelope that must occur to accommodate perinuclear viral particles. Viral capsids were also observed in the cytoplasm in close proximity to vesicles that are likely sites of secondary envelopment (**Fig. 1G**). After secretion, HSV-1 particles commonly remain bound to the cell surface, a property that may be exacerbated by the antiviral restriction factor tetherin[32,33]. In addition, we expected to see HSV-1 particles between cells because virions are targeted to cell junctions to promote cell-cell spread[34]. Linear arrays of dark puncta were observed on the cell surface and between cells (**Fig. 1H & I**) and likely represent released virus particles (extracellular virions). Virus particles accumulate most of their tegument in the cytoplasm and become enveloped before they are released from the cell. We measured the width of nuclear capsids and extracellular virions from 8 tomograms to determine if they could be distinguished based on their size (**Fig. 1J**). Nuclear capsids had a width of 125.8 ± 1.70 nm SEM (n=80 from 4 tomograms; range 96–160 nm; SD 15.22 nm), which is consistent with high-resolution structural analysis of purified capsids[29] (~125 nm) and of capsids inside infected-cell nuclei[35]. Extracellular virions were larger with a width of 198.6 ± 3.48 nm SEM (n=80 from 4 tomograms; range 128–272 nm; SD 31.15 nm), consistent with previous reports (~175-200 nm[28,36]). These differences were found to be significant with a Wilcox test for unequal variance (W=126, *p*-value<2.2×10^{-16}).

Early protein ICP0 and late protein gC have different patterns of spatiotemporal expression in HFF-hTERT and U2OS cells

Recent microscopy and single-cell transcriptomics studies have revealed that, even in a monolayer of cultured cells synchronously infected with HSV-1, individual cells progress through the infection cycle at different rates and the remodelling of cellular compartments varies depending on the stage of infection[16,37]. To control for this, a recombinant strain of HSV-1 termed the timestamp virus has been developed to allow identification of the stage of infection based on the abundance and subcellular localization of the fluorescently tagged early and late viral proteins, ICP0 and gC respectively[16]. Fluorescence microscopy of HFF-hTERT cells infected with this timestamp virus allowed characterization of the changes to cellular compartments that accompany progressing HSV-1 infection and categorization of cells into 4 stages of infection. Having confirmed that virus particles could be observed in infected HFF-hTERT cells using a 40 nm zone plate objective, we sought to obtain higher-resolution information on the morphological changes exhibited by timestamp HSV-1-infected cells over the course of infection by cryoSXT imaging using a 25 nm zone plate objective. However, preliminary experiments performed using infected HFF-hTERT cells were unsuccessful as the infected cells proved sensitive to higher flux density of the resultant X-ray beam, leading to localized sample heating and low-quality tomograms. We therefore turned to U2OS osteosarcoma cells, which have been shown to produce consistently high-quality tomograms when imaged by cryoSXT[25,26] and have been used previously for HSV-1 ultrastructural analysis[38,39].

To compare the temporal profiles of progression of timestamp HSV-1 infection in HFF-hTERT and U2OS cells, we first compared the expression patterns of these proteins between the two cell types. Cells were infected at a multiplicity of infection (MOI) of 1 and 3 and samples were fixed at multiple time points following infection before imaging on a widefield fluorescence microscope (**Fig. 2**). The immediate early HSV-1 protein ICP0 was used to characterize early stages of infection because it is one of the first viral proteins to be expressed[40]. In both cell lines, eYFP-ICP0 was expressed in all four stages and its localization was restricted to the nucleus in stage 1. However, the spatial localization of eYFP-ICP0 differed between HFF-hTERT and U2OS cells in stages 2-4: in these stages of HFF-hTERT cell infection, eYFP-ICP0 signal was observed to diminish in the nucleus and continue to increase in the cytoplasm across these three stages, whereas greater retention of eYFP-ICP0 in the nucleus was

observed in U2OS cells throughout the entire course of infection (**Fig. 2A**). This may reflect differences in cellular interactions for ICP0 in U2OS cells, which is consistent with previous observations demonstrating that replication deficits demonstrated by ICP0-null strains of HSV-1 in human fibroblasts are effectively complemented in U2OS cells[41]. Unlike eYFP-ICP0, the spatial expression of gC-mCherry was similar between HFF-hTERT and U2OS cells. gC is a viral glycoprotein expressed at late stages of virus replication[42] that is incorporated into nascent virus particles at sites of virus envelopment[43]. In both cell types gC-mCherry was enriched at a juxtanuclear site in stage 3 but became dispersed throughout the cytoplasm and at the plasma membrane by stage 4 (**Fig. 2A**).

Next, we probed whether progression through the replication cycle follows the same timecourse in HFF-hTERT and U2OS cells by infecting with different MOIs and imaging at different times post-infection to compare the proportion of infected cells at each stage of infection. Although the spatial expression of gC-mCherry was similar, fewer U2OS cells transitioned between stages 3 and 4 compared to HFF-hTERT cells at MOI 1 and 3, even by the 24-hour timepoint (**Fig. 2B**). Stage 4 is defined by the dispersal of gC-mCherry throughout the cytoplasm and, given the colocalization of gC with Golgi markers 58K protein and beta-1,4-galactosyltransferase 1, this dispersal is thought to arise via fragmentation of the Golgi complex[16]. The reduced number of U2OS cells in stage 4 may suggest a delay in, or resistance to, Golgi complex fragmentation. The partial cytoplasmic translocation of eYFP-ICP0 and the reduced gC-mCherry dispersal complicated the distinction between stages 1 and 2, and between stages 3 and 4, respectively. As a result, we combined the stages into two broader early (1+2) and late (3+4) stages in our study.

Vesicles proliferate and mitochondria become elongated and branched during HSV-1 infection.

To characterize the changes in morphology of cellular compartments that accompany different stages of virus infection, U2OS cells were grown on holey-carbon EM grids before being infected (or mock infected) with timestamp HSV-1 and cryogenically preserved by plunge freezing in liquid nitrogen-cooled liquid ethane (**Fig. 3A**). Vitrified samples were analyzed by cryo-wide-field microscopy to classify the stage of infection and then imaged using cryoSXT to correlate the stage of virus infection in a specific cell with observed morphological changes (**Fig. 3B**). As the proportion of U2OS cells in the early stages of infection (stages 1+2) was consistently lower than the proportion in late stages of

infection (stages 3+4; **Fig. 2B**), grids were infected at MOI 1 and plunge frozen at 9 hpi to achieve a more balanced proportion of cells in early and late stages of infection.

In total, 139 SXT tomograms were reconstructed; 76 from uninfected cells alongside 22 and 41 from cells at early- or late-stages of infection, respectively, across three independent replicates (**Table 1**). Manual inspection of the resultant tomograms revealed that the 25 nm zone plate allows detection of higher resolution features than is possible with the 40 nm zone plate, such as the lumen of the endoplasmic reticulum, cytoskeletal filaments, and small membrane structures (**Supp. Fig. 1A-E**). The observed width of nuclear capsids is very similar in infected HFF-hTERT cells imaged using the 40 nm zone plate (**Fig. 1J**) or U2OS cells imaged using the 25 nm zone plate (**Supp. Fig. 1F**). The tomograms collected from U2OS cells using the 25 nm zone plate were thus deemed suitable for identifying changes to cellular compartments that occur during HSV-1 infection.

We observed that the HSV-1 infection does not affect the morphology of cellular compartments such as the nucleus and lipid droplets. Despite the continuous budding and fusion of capsids at the inner and outer nuclear membranes, we did not observe any obvious changes to the integrity of the nuclear envelope. We occasionally observed bulging of the nuclear envelope into the cytoplasm (**Supp. Fig. 1G**) but this could be seen in both uninfected and infected cells. The size and abundance of lipid droplets did not appear to differ between uninfected, cells and those at early- or late-stages of infection. However, striking changes were observed in the size and dispersal of vesicles, and in the length and connectivity of the mitochondrial network, between uninfected and infected cells, with the changes becoming more pronounced in cells at late stages of infection (**Fig. 4&5 and Supp. Video 1**).

HSV-1 capsids are thought to interact with several types of vesicles in the cytoplasm, including *trans*-Golgi network vesicles and endosomes, both of which have been implicated in secondary envelopment[13]. There was a striking difference in the concentration of vesicles at the juxtanuclear compartment between uninfected and infected cells (**Fig. 4A and Supp. Video 2**). Infected cells had a greater number of vesicles in juxtanuclear regions than uninfected cells. To determine if there was a difference in the size of vesicles between uninfected cells and those at early- or late-stages of infection we developed *Contour*, a program to segment and quantitate cellular features in 3D volumes (manuscript in preparation). The widest point of each vesicle in three dimensions from 4 tomograms for each condition was measured (**Fig. 4B**). The mean vesicle width was higher for uninfected cells (802.23

± 348.47 nm SD, N=96) than for early-stage (688.66 ± 271.76 nm SD, N=184) and late-stage (631.85 ± 270.60 nm SD, N=184) infected cells. The mean vesicle widths for each tomogram were compared using a one-way ANOVA and Tukey test and the vesicle widths of uninfected cells were found to be significantly different from early-stage ($p=0.04$) and late-stage ($p=0.01$) infected cells. The vesicle width did not differ significantly between early-stage and late-stage infected cells ($p=0.62$).

Mitochondria were the most phenotypically diverse organelles monitored in this study. In most cases, they were thin and possessed a dark matrix (**Fig. 5A**). However, occasionally there were cells that contained swollen mitochondria with a lighter matrix with highly contrasting cristae (**Supp. Fig. 2A**), similar to observations of mitochondria made by EM[44–46]. This swollen morphology is associated with release of cytochrome *c* from porous mitochondria during apoptosis[44]. Mitochondria are known to interact with lipid droplets, for example to acquire fatty acids for respiration[47]. Interestingly, we observed that lipid droplets were less frequently in close apposition to swollen mitochondria than to mitochondria possessing dark matrices (**Supp. Fig. 2B**). Swollen mitochondria were observed in each of the three independent sets of cell growth, infection and plunge freezing experiments performed, but these swollen mitochondria were most prevalent in the uninfected cells of replicate 3 (**Supp. Fig. 2C**). In uninfected cells, non-swollen mitochondria were heterogeneous in shape, with numerous being small and spherical or long and curved in the same cell. We observed branching in some elongated mitochondria. However, mitochondria appeared less heterogenous in shape in infected cells, and were consistently more elongated and branched (**Fig. 5B and C, Supp. Fig. 2D,** and **Supp. Video 3**), in line with previous observations made using super-resolution fluorescence microscopy of HFF-hTERT cells infected with the timestamp virus[16]. Segmentation of mitochondria using *Contour* demonstrated that the number of points where mitochondria branch into two or more arms (branching nodes) was significantly increased in cells at late stages of infection (20.5 ± 5.45 nodes SD; n = 15) compared to uninfected cells (7.0 ± 4.02 nodes SD; n = 15) (**Fig. 5C**). In some cases, the mitochondria fused into a single, branched network (**Fig. 5A** and **Supp. Video 3**), providing a dramatic demonstration of the increase in mitochondrial branching and decrease in number of distinct mitochondrial networks that accompanies HSV-1 infection. It was also observed that the number of distinct mitochondria decreased in infected cells, although ambiguity regarding the connectivity of mitochondrial networks that extend beyond the tomogram field-of-view prevented precise quantitation of this effect.

Discussion

In this study, we used cryoSXT to monitor the production of nascent HSV-1 particles and observe changes in the architecture of cellular compartments during infection. The penetrating power of X-rays facilitates cryoSXT imaging throughout the depth of the cell, allowing rare or transient events to be captured such as the transit of nascent capsids through the nuclear envelope. Furthermore, the lack of requirement for contrast-enhancing agents or chemical fixation allows direct imaging of cellular compartments in a near-native state. We exploited these properties of cryoSXT to compare the morphology of cellular compartments between uninfected and infected U2OS cells, using a recombinant strain of HSV-1 expressing fluorescently tagged early and late viral proteins to identify the infection stage of individual cells within the infected population.

HFF-hTERT and U2OS cells are commonly used for the study of HSV-1 infection[16,38,39]. We had intended to use HFF-hTERT cells for this study, to allow comparison with super-resolution fluorescence microscopy studies[16], but found infected HFF-hTERT cells to be less amenable to interrogation by cryoSXT. We therefore explored the differences in the dynamics of viral infection between HFF-hTERT and U2OS cells using the timestamp virus. In general, the modifications to cellular compartments observed in this study largely replicated those observed in HFF-hTERT cells[16], suggesting the interactions between viral components and cellular compartments are broadly similar in these two cell types. We observed subtle differences between the infections in these cells, including a U2OS-specific reduction in the dispersion of gC-containing membranes and a change in the nuclear-to-cytoplasmic translocation of the early viral protein ICP0 (**Fig. 2**). Residues important for the nuclear import/export dynamics of ICP0 have previously been identified: ICP0 possesses a canonical nuclear localization signal at residues 500–506 and deletion of 57 residues from the C terminus abolishes nuclear export of ICP0[48]. Although residues important for trafficking of ICP0 have been mapped, the cellular proteins involved in ICP0 trafficking have yet to be identified. In this study, a higher intensity of eYFP-ICP0 was detected in the nucleus compared with the cytoplasm of infected U2OS cells at every timepoint. In contrast, higher cytoplasmic intensity of ICP0 is observed at late stages of infection in HFF-hTERT cells and other cell lines[16,49,50]. This suggests that the expression of host proteins that regulate nuclear import and/or export of ICP0 may differ in U2OS cells. Several host proteins have been identified to participate in the nuclear trafficking of EP0, the pseudorabies virus orthologue of ICP0: Ran, Importin α1, α3, α7,

β1, and transportin-1[51]. Future work is required to identify whether U2OS cells are depleted or enriched in proteins involved in nuclear import/export of ICP0, which may illuminate the mechanisms regulating subcellular localisation of this important viral E3 ligase during infection.

Compared with uninfected U2OS cells, infected cells had a greater local concentration of detectable vesicles in the juxtanuclear space (Figure 4), consistent with previous research into the distribution of vesicles during HSV-1 infection. For instance, early endosomes and lysosomes have been shown to accumulate at the juxtanuclear region during infection[16]. This reorganization of vesicle distribution may be related to a change in microtubule dynamics during infection. Previous studies have shown that γ-tubulin and pericentrin, which are components of the microtubule-organizing centre (MTOC), become dispersed during infection, suggesting breakdown of the MTOC[52]. Thereafter microtubules polymerize at multiple foci in the cytoplasm rather than at a single site and the growth rate, length, and stability of nascent microtubules become reduced compared with uninfected cells[52]. As the morphology of microtubules changes, the transport of vesicles towards the cell periphery may be obstructed, resulting in the accumulation of vesicles in juxtanuclear regions that may partly explain the increased local concentration of vesicles. An additional source of new vesicles may arise from the fragmentation of the Golgi complex during HSV-1 infection[53]. Most of the evidence for Golgi fragmentation is based on the dispersion of several Golgi markers (β-COP, Giantin, GM130, 58K protein, and beta-1,4-galactosyltransferase 1) throughout the cytoplasm during HSV-1 infection as assessed by fluorescence microscopy[16,17,53]. Golgi fragmentation has been studied to a lesser extent by ultrathin section EM, revealing cisternae become swollen and separated during infection[17]. Golgi fragmentation is thought to be a consequence of disrupted microtubule dynamics and can be induced by treatment with nocodazole, an inhibitor of β-tubulin polymerization[53]. Although our results are consistent with these observations, the lack of markers for different types of vesicles meant that we could not determine if the vesicles we observed with SXT were Golgi-derived, of endosomal origin, or were unrelated to these cellular compartments. We observed a reduction in the mean size of vesicles as the infection progressed (Figure 4B), which could arise either from fragmentation of the Golgi complex into small vesicles or an inability of small vesicles to be trafficked from the juxtanuclear region to their target organelles via microtubule transport. Future work could focus on the use of fluorescent markers and

correlative cryoSIM and cryoSXT imaging to identify which cellular compartments are found with an increased concentration at the juxtanuclear region[25,54].

The spatial resolution afforded by cryoSXT allowed us to easily distinguish individual mitochondria in uninfected and infected U2OS cells. Consistent with previous studies of infected HFF-hTERT cells[16], we observed that mitochondria became more elongated and branched as infection progresses and form extensive networks in some cases (Figure 5). Branching of mitochondria can either occur via *de novo* synthesis or by fusion of mitochondria[55,56]. Our observation that some cells at late stages of infection contain just one single large network of mitochondria, rather than numerous highly branched but disconnected mitochondrial networks, is consistent with fusion predominating over fission as a driver of mitochondrial network formation.

There are several possible explanations for the change in mitochondrial morphology observed during HSV-1 infection. Mitochondrial movement tends to occur along microtubules and this movement influences mitochondrial fusion/fission dynamics. Fission can arise from divergent movement of mitochondrial extensions along microtubules and fusion is supported by convergent movement of mitochondria[57]. Nocodazole treatment to depolymerize microtubules blocks transport, fusion and fission of mitochondria, and there is evidence that thin microtubule extensions develop when fission is obstructed[58]. It is possible that fission of existing mitochondrial networks may be obstructed when microtubules depolymerize during HSV-1 infection, and this may prevent the generation of small mitochondria. Such changes to the microtubule network begin at 6 hpi and would thus be expected to have a greater influence on mitochondrial morphology in the late stages of infection[52], consistent with our observations. Alternatively, the morphological changes to mitochondria may reflect a cellular response to increased respiratory demand[59]. An increase in ATP production can be achieved by mitochondrial elongation, for example under conditions of stress such as hypoxia and starvation of glucose metabolism[60,61]. An increase in respiration, including oxidative phosphorylation, has been observed for the related herpesvirus human cytomegalovirus[62]. The increased number of elongated mitochondria in cells at late stages of infection could facilitate an increase in ATP production during infection. Increased oxidative stress provides a third plausible explanation for the observed changes in mitochondrial morphology. Increased production of reactive oxygen species (ROS) during respiration appears to be a common feature of viral infection that has been observed for hepatitis C virus,

372 respiratory syncytial virus and the herpesvirus Epstein-Barr virus[63–65]. One mechanism by which the
373 cell responds to oxidative stress is by fusion of undamaged and ROS-damaged mitochondria to allow
374 for compensatory effects by sharing resources needed for ATP production[56]. It is possible that the
375 increased fusion events we observed may have arisen in response to increased oxidative stress during
376 infection.

377 Although a change in energy metabolism may reflect a generalized response by the cell to infection,
378 several HSV-1 proteins have been reported to localize at mitochondria (pUL7, pUL16, pUS3,
379 pUL12.5), suggesting that HSV-1 directly modulates mitochondrial activity[66–69]. pUS3 inhibits the
380 activity of electron transport chain complexes II and III as early as 6 hpi[67] and pUL12.5 functions in
381 the depletion of mitochondrial DNA and downregulation of mitochondrial proteins, including ND6 and
382 COX2, as early as 4–8 hpi[68]. The functional consequences of pUL16 binding mitochondria are not
383 well characterized, although we note that a pUL16 mutant co-localized with mitochondrial fission
384 sites[69]. The precise mechanisms by which HSV-1 alters the architecture of mitochondria and the role
385 of specific viral proteins, versus virus-induced metabolic strain, thus remains unclear. Combining
386 metabolic profiling of infected cells with ultrastructural analysis of mitochondrial morphology, using
387 wild-type and mutant (knock-out) viruses, will help illuminate the factors that drive the dramatic
388 remodelling of mitochondria observed during HSV-1 infection and the functional consequences
389 thereof.

390 In conclusion, cryoSXT allows the detection HSV-1 capsids and virions in different subcellular locations,
391 such as the nucleus, perinuclear space, cytoplasmic vesicles, and cell surface. Use of the timestamp
392 HSV-1 reporter virus facilitated identification of individual cells at early or late stages of infection, and
393 we observed accumulation of vesicles at juxtanuclear assembly compartments plus the elongation and
394 branching of mitochondria in infected cells as infection progresses. The ability of cryoSXT to image the
395 entire depth of infected cells in a near-native state, with minimal sample processing, highlights its utility
396 as a tool for 3D imaging to identify changes in cellular architecture that accompany virus infection.

397

398

Materials & Methods

Reagents

250 nm gold colloid fiducials were purchased from BBI Solutions (EM.GC250, batch 026935). The working mixture was prepared via sedimentation of 1 mL of stock solution by centrifugation (12×g, 5 mins, RT) and then resuspending the pellet in 50 µL HBSS. The fiducials were sonicated at 80 kHz (100% power) and 6°C to prevent aggregation. 3 mm gold EM grids with a holey carbon film (R 2/2, 200 mesh) were purchased from Quantifoil (Cat# AU G200F1 finder, batches Q45352 & Q45353). Poly-L-lysine was purchased from Sigma Aldrich (Cat# P4832).

Cell Lines

U2OS cells (ATCC HTB-96; RRID CVCL_0042) and human foreskin fibroblast cells immortalized with human telomerase reverse transcriptase (HFF-hTERT cells)[70] were cultured in Dulbecco's Modified Eagle's Medium (DMEM; Thermo Fisher Scientific, Cat# 450 11590366) supplemented with 10% (v/v) fetal bovine serum (FBS; Capricorn, Cat#: FBS-11A), L-glutamine (Thermo Fisher Scientific, Cat# 25030081), and penicillin/streptomycin (10000 U/ml; Thermo Fisher Scientific, Cat# 15070063). Hanks' Balanced Salt Solution (HBSS; Thermo Fisher Scientific, Cat# 14175095) and 0.25% Trypsin-EDTA (Thermo Fisher Scientific, Cat# 25200056) were used to wash and detach adherent cells, respectively. Cells were maintained in a humidified 5% CO_2 atmosphere at 37°C.

Recombinant Viruses

Infections were performed using recombinant HSV-1 strain KOS expressing either the endogenously tagged viral proteins eYFP-VP26 and gM-mCherry (Figure 1) or the endogenously tagged viral proteins eYFP-ICP0 and gC-mCherry (timestamp HSV-1, Figures 2-5 and Supplementary Figures 1-2)[16], to allow distinction between early and late stages of infection in U2OS and HFF-hTERT cells, with the exception of the leftmost panel in **Fig. 1I** for which a non-fluorescent wild-type HSV-1 strain KOS was used. Virus stocks were prepared by infection of Vero cells at low MOI (0.01) for 3–5 days, until cytopathic effect was evident, before scraping cells into the medium. The cells were frozen at -70°C, thawed and sonicated at 50 amps for 40 seconds. Crude virus stocks were clarified by centrifugation at 3,200×g in a benchtop centrifuge, aliquoted, and viral titers of the aliquots were quantified on Vero and U2OS cells as described previously (71).

Infection Assays

For widefield imaging at ambient temperatures, HFF-hTERT and U2OS cells were seeded directly in 6-well plates overnight at 2×10^5 cells per well. The cells were infected with the recombinant HSV-1 at 1–3 PFU per cell in a low volume of media (500 µL) and this was designated as the start time of infection. To maximize adsorption of virus, cells were incubated in the low-volume media for 1 hour in a humidified 5% CO_2 atmosphere at 37°C and the plates were swirled every 15 minutes. The inoculum was diluted to 2 mL with medium and cells were incubated for 9-, 12-, 16- or 24-hours in total. The cells were washed twice with HBSS and were fixed with 4% (v/v) formaldehyde for 20 minutes. The fixed cells were washed three times with HBSS before imaging.

For widefield imaging under cryogenic conditions and cryoSXT, EM grids were glow discharged and treated with filtered poly-L-lysine for 10 minutes as described previously (26). 3×10^5 cells per well were seeded in 6-well plates containing the treated EM grids and were incubated overnight. Subsequently, the cells were infected with 1 PFU per cell of timestamp HSV-1 as described above and were incubated for 9 hours alongside uninfected controls. The EM grids were overlayed with 2 µL of the gold fiducial working mixture described in the Reagents section. A Leica EM GP2 plunge freezer was used to blot the grids for 0.5–1 s at 30°C and 80% humidity. The grids were plunged into liquid nitrogen-cooled liquid ethane and then transferred into liquid nitrogen storage before imaging.

Widefield Microscopy

For room temperature samples, a Zeiss AxioImager2 microscope with an achromatic 50× air objective (Zeiss LD EC Epiplan-Neofluar 50x/0.55 DIC M27; NA=0.55; free working distance=9.1 mm) was used to image fixed infected cells grown on plastic 6-well plates. Fluorescent images were collected using the Zeiss 46 HE YFP filter (Excitation 500±25 nm, Emission 535±30 nm) and the Zeiss 64 HE mPlum filter (Excitation 587±25 nm, Emission 647±70 nm).

For cryo-widefield microscopy, cells at early- and late-stages of infection were identified based on the spatiotemporal expression of eYFP-ICP0 and gC-mCherry using a Zeiss AxioImager2 microscope with an achromatic 50× objective (described above) without immersion. The microscope was equipped with a liquid nitrogen cryostage (Linkam) to maintain the sample at 77 K during imaging. Each grid was

mapped in its entirety in the brightfield and fluorescent channels (Zeiss 46 HE YFP filter and HE mPlum filter as described above) using the LINK software (Linkam Scientific).

Cryo-Soft-X-Ray Tomography

X-ray images were collected using an UltraXRM-S/L220c X-ray microscope (Carl Zeiss X-ray Microscopy) at beamline B24 at the UK synchrotron Diamond Light Source. Grids were imaged in a liquid nitrogen-cooled vacuum chamber and samples were illuminated with 500 eV X-rays (λ = 2.48 nm) for 0.5 or 1 s per projection. The transmitted light was focused by diffraction using zone plate objectives with nominal resolution limits of either 25 nm or 40 nm. The 25 nm zone plate offers higher resolution but captures a smaller field of view (~10×10 μm) than the 40 nm zone plate (~16×16 μm). Transmitted images were collected using a 1024B Pixis CCD camera (Princeton instruments). X-ray mosaic images (7×7 images capturing 66.2×66.2 μm for the 25 nm objective and 106.0×106.0 μm for the 40 nm objective) were collected from different areas on the grid to assess overall cell morphology. For identification of early and late stages of infection, X-ray mosaics were compared with fluorescent imaged acquired on the cryo-widefield microscope to identify specific infected cells. These mosaics were also used to identify regions of interest for tomography. Tilt series of projections were collected from these regions by rotating the sample around an axis normal to the incident X-ray beam by up to 120° in increments of 0.2° or 0.5° per image, with maximum tilt angles of −60° and +60° and −70° and +70° for the 25nm and 40nm objective respectively. SXT tilt series were processed using IMOD (version 4.9.2)[31]. The images were aligned along a single axis. A coarse alignment was performed by cross-correlation with a high frequency cut-off radius of 0.1. Coarsely aligned tilt series were further aligned manually using gold fiducials and dark cellular compartments, such as lipid droplets. A boundary model was generated to reorient the 3D data in case the sample was collected at an angle and final alignment was performed using linear interpolation. Tomograms were generated using back projection followed by 20 iterations of a simultaneous iterations reconstruction technique (SIRT)-like filter to reduce noise.

Segmentation

Mitochondria were segmented using *Contour*, a bespoke semi-automated segmentation and quantitation tool developed with Python 3. Full details on *Contour* will be described elsewhere but, briefly, *Contour* automatically segments high contrast features such as mitochondria by thresholding and then applying a restriction on the minimum number of consecutive segmented pixels vertically and

horizontally. Next, gaps in the segmented volume can be filled in by running this algorithm in local regions of interest. Separate elements in the segmented volume are differentiated by grouping of neighbouring voxels together. The differentiated elements are colour coded and their volumes are quantitated from the number of voxels. The edges of the segmented elements are smoothened in each image plane by translating the image by one pixel in all eight cardinal and ordinal directions in the XY plane and calculating the median pixel value for all these translations. A 3D Gaussian filter with a sigma of 2 was also added using Fiji to further smoothen the elements[72]. In *Contour*, the width of each segmented element was calculated by finding all the coordinates of voxels at the perimeter of segmented elements and calculating the largest modulus between any two coordinates. Segmented volumes of cytoplasmic vesicles were generated manually using the Segmentation Editor 3.0.3 ImageJ plugin[72] and these were imported into *Contour* to differentiate between segmented elements and quantitate the width of the vesicles. Segmented volumes were visualized in 3D using the 3D Viewer plugin in ImageJ[72].

Graphs and statistics

Distributions of capsid and virion widths were illustrated using a Violin SuperPlot[73], with data grouped by source tomograms. The stacked area plots for the proportion of infected cells at different stages of infection were generated using the ggplot2 package[74] in R studio[75]. The distribution of vesicle widths were illustrated using a SuperPlot[76], with data grouped by source tomograms. The numbers of mitochondrial branch points (branching nodes) were illustrated using a Violin SuperPlot[73], with data grouped by replicate. A two-tailed paired t-test was used to compare the width of the nuclear envelope at a site of primary envelopment with the width of the nuclear envelope elsewhere on the same tomogram using Excel (Microsoft). A Wilcox test for unequal variance was used to assess a significant difference in the widths of capsids and virions using R Studio[75]. One-way ANOVA and Tukey tests were used to assess significant differences in the mean vesicle width using Prism version 8.2.1 (GraphPad Software) and in the number of mitochondrial branching nodes (using R Studio[75]).

Acknowledgements

We thank Diamond Light Source for access to beamline B24 (mx18925, mx19958, bi21485 and bi23508) and the experimental hall coordinators for helpful support. We thank members of beamline B24 at the Diamond Light Source (Mohamed Koronfel, Ilias Kounatidis, Chidinma Okalo, and Matt Spink) for technical support with cryoSXT. We thank João Ferreira Fernandes (University of Oxford) and Thomas Fish (Diamond Light Source) for help with the development of *Contour*. We thank Harriet Groom (University of Cambridge) for reading and advising on the manuscript. This work was supported by a PhD studentship co-funded by Diamond Light Source and the Department of Pathology, University of Cambridge, to KLN, by a Biotechnology and Biological Sciences Research Council (BBSRC) Research Grant to CMC (BB/M021424/1), and by a Sir Henry Dale Fellowship, jointly funded by the Wellcome Trust and the Royal Society, to SCG (098406/Z/12/B).

Data Availability

Original imaging data for tomograms illustrated in the manuscript is deposited at the BioImage Archive (https://www.ebi.ac.uk/biostudies/BioImages) and EMPIAR (https://www.ebi.ac.uk/pdbe/emdb/empiar/). The accession numbers for the data are EMPIAR: EMPIAR-XXXX, EMPIAR-XXXX, … and BioImage Archive: S-BIADXX, S-BIADXX, …. Additional tilt series and tomograms used for quantitative analysis have been deposited with the University of Cambridge Apollo Repository, available at https://doi.org/10.17863/CAM.XXXX.

527 **Table 1. Collection of cryoSXT data to analyse changes in cellular morphology accompanying**
528 **infection.** CryoSXT data was collected using a 25 nm zone plate from multiple uninfected cells or cells
529 at early and late stages of infection across three independent replicates. Tiled X-ray projections ('X-ray
530 mosaics') with a 66.2×66.2 μm field of view were collected at multiple areas on the sample grid to
531 identify cells of interest. Tilt series were collected at perinuclear or peripheral regions of the cytoplasm
532 within these cells and were processed to generate tomograms.

Replicate	Stage of infection	X-ray mosaics	Cells in mosaics	Cells imaged by tomography	Tomograms
1	Uninfected	19	30	18	29
	Early	4	4	2	4
	Late	8	13	10	14
2	Uninfected	10	20	14	20
	Early	9	13	11	13
	Late	10	10	8	12
3	Uninfected	8	27	26	27
	Early	6	7	5	5
	Late	8	13	13	15

533

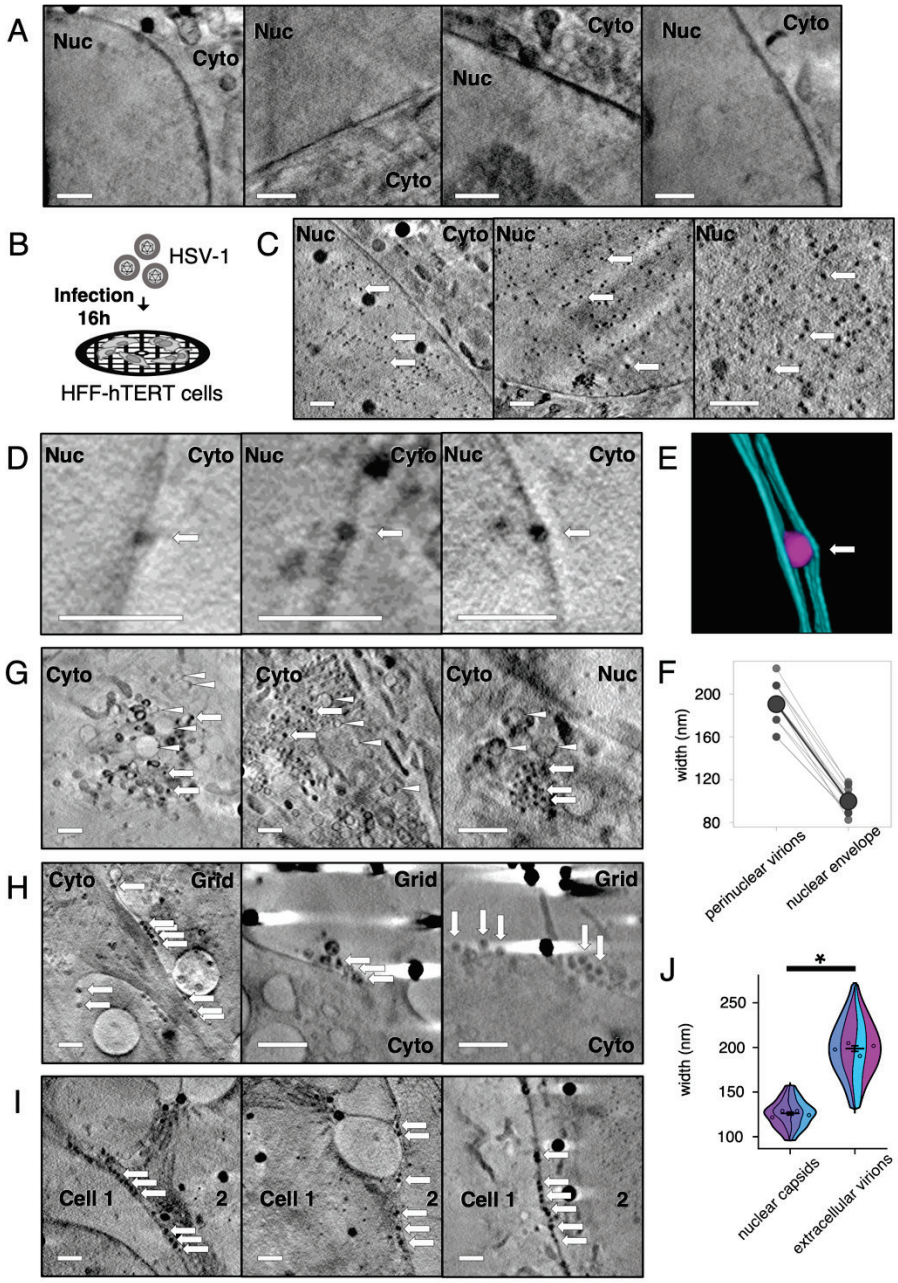

534

535 **Fig. 1. Soft X-ray tomography imaging at cryogenic temperatures of HSV-1-infected HFF-hTERT**
536 **cells identifies virus particles.** HFF-hTERT cells were grown on EM grids and plunge frozen 16 hpi
537 with 2 plaque-forming units of HSV-1 per cell or mock infection. All tomograms were reconstructed from
538 X-ray projections collected using zone plate objective optics affording 25 nm (**A**) or 40 nm (**C, D, G–I**)
539 resolution; scale bars = 1 μm. (**A**) The nucleus (Nuc) has a largely uniform X-ray absorbance in
540 uninfected HFF-hTERT cells. Cyto, cytoplasm. (**B**) Schematic of infection workflow. (**C**) In HSV-1
541 infected cells many dark puncta are evident in the nucleus, consistent with these puncta being newly
542 assembled HSV-1 capsids. (**D**) Dark puncta were also observed within the perinuclear space of the

nuclear envelope, consistent with these being HSV-1 capsids undergoing primary envelopment/de-envelopment to leave the nuclear space. (**E**) Segmentation of a perinuclear viral particle (magenta) and the two membranes of the nuclear envelope (cyan). The perinuclear viral particle distends the nuclear envelope. (**F**) The width of perinuclear viral particles plus associated membranes is 190.5 ± 6.01 nm SEM (N=11; 20.8 nm SD), which is greater than the width of the nuclear membrane elsewhere (99.8 ± 3.57 nm SEM; N=11; 11.9 nm SD). (**G**) HSV-1 capsids (arrows) were also observed in the cytoplasm alongside vesicles (arrowheads). (**H**) Multiple particles are observed along the surface of infected cells, consistent with these being assembled HSV-1 virions that have exited the infected cell. (**I**) HSV-1 virions are also observed at the junctions between cells. (**J**) The width of the nuclear capsids is 125.8 ± 1.70 nm SEM (n=80 from 4 tomograms), consistent with these being HSV-1 capsids (~125 nm[28,29]). The width of the extracellular virions is 198.6 ± 3.48 nm SEM (n=80 from 4 tomograms), consistent with these being fully-enveloped HSV-1 virions (~200 nm[36]). Due to unequal variance, a Wilcox test was performed to determine a significant difference in the width of nuclear capsids and extracellular virions ($W=126$, p-value$<2.2\times10^{-16}$). Error bars show mean ± SEM.

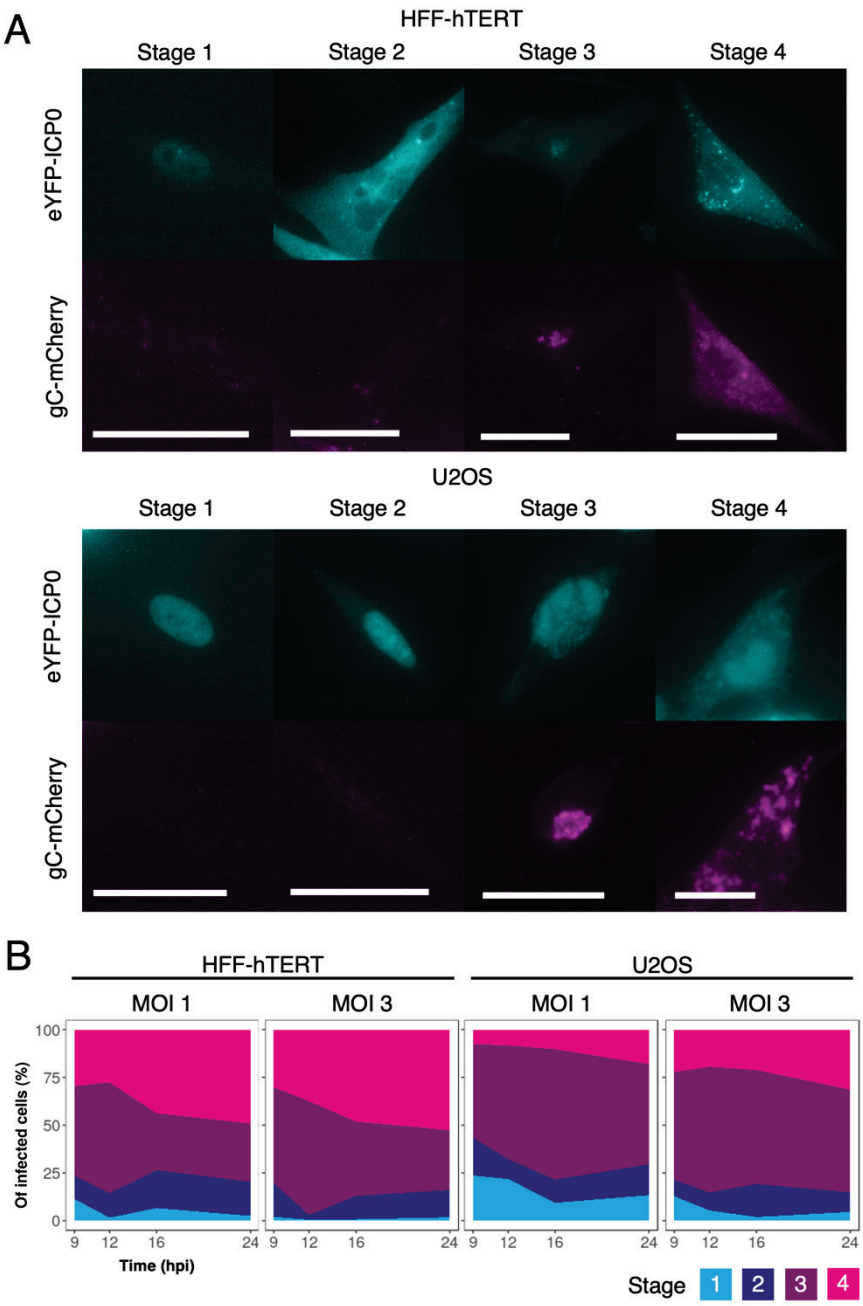

Fig. 2. Temporal analysis of HSV-1 infection using the dual-fluorescent timestamp virus. (**A**) Room temperature widefield fluorescence imaging of timestamp HSV-1 infected HFF-hTERT and U2OS cells was used to delineate between four stages of infection based on the expression and localization of the early protein eYFP-ICP0 and the late protein gC-mCherry[16]. The spatiotemporal expression of these fusion proteins was similar in HFF-hTERT and U2OS cells, except for partial retention of eYFP-ICP0 in the nucleus of U2OS cells during stages 2–4. Scale bars = 50 μm. (**B**) The proportion of infected cells in each stage was determined using widefield imaging and different multiplicities of infection (MOIs) in HFF-hTERT and U2OS cells at 9, 12, 16, and 24 hpi.

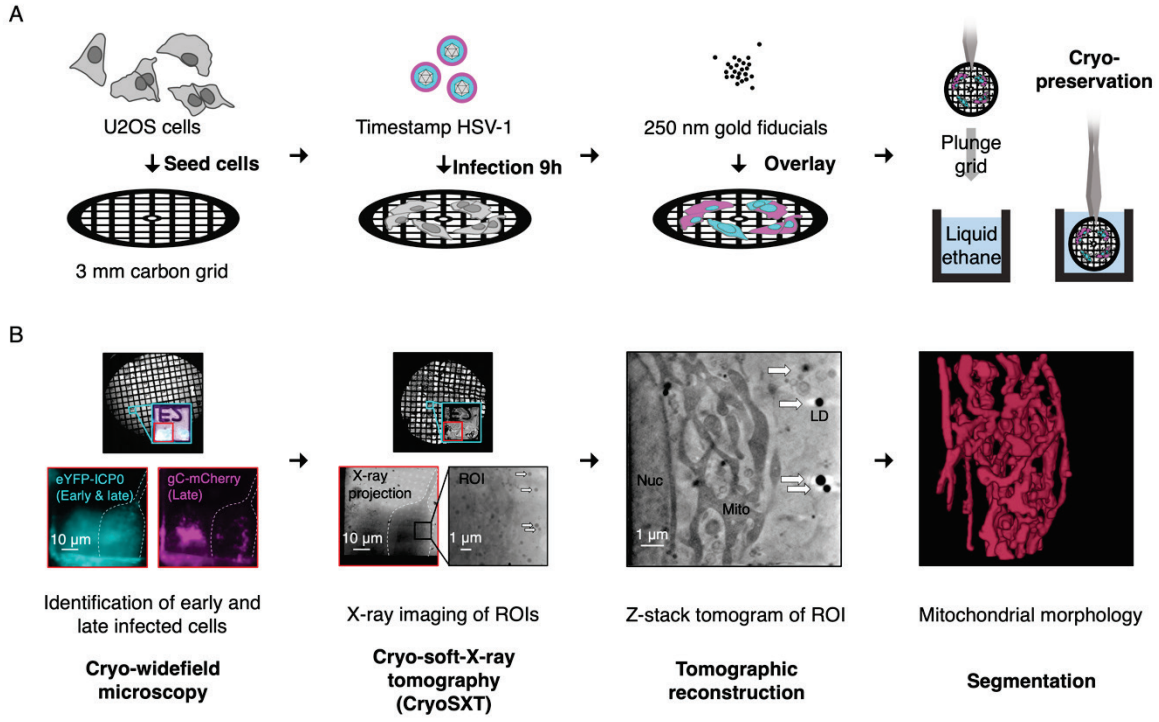

Fig. 3. Workflow for multi-modal imaging of HSV-1 infected cells. (**A**) Preparation of infected cells samples for multimodal imaging. U2OS cells are cultured on holey-carbon EM grids and infected with recombinant 'timestamp' HSV-1, expressing fluorescently tagged proteins eYFP-ICP0 and gC-mCherry that allow identification of the stage of infection for each cell under investigation. At 9 hpi, gold fiducials are overlayed onto the sample to facilitate image registration and grids are cryopreserved in a near-native state by plunge freezing in liquid ethane. (**B**) Multi-modal imaging of infected U2OS cells. A widefield microscope with a cryo stage is used to locate the grid positions of infected cells. The stage of infection for each cell is determined based on the differential expression and localisation of the eYFP-ICP0 and gC-mCherry (as shown in **Fig. 2**). These grids are then loaded into the cryo-soft-X-ray microscope at Diamond Light Source beamline B24 and are illuminated with soft X-rays at the marked grid positions. X-ray projections of regions of interest (ROIs) are collected at multiple angles and aligned using the gold fiducials and intracellular features, such as lipid droplets (LDs), with the program IMOD[31]. Tomograms are reconstructed from these projections using IMOD to compare intracellular morphology between uninfected cells and those at early- or late-stages of infection. Segmentation facilitates quantitation and visualization in three dimensions of the observed cellular structures.

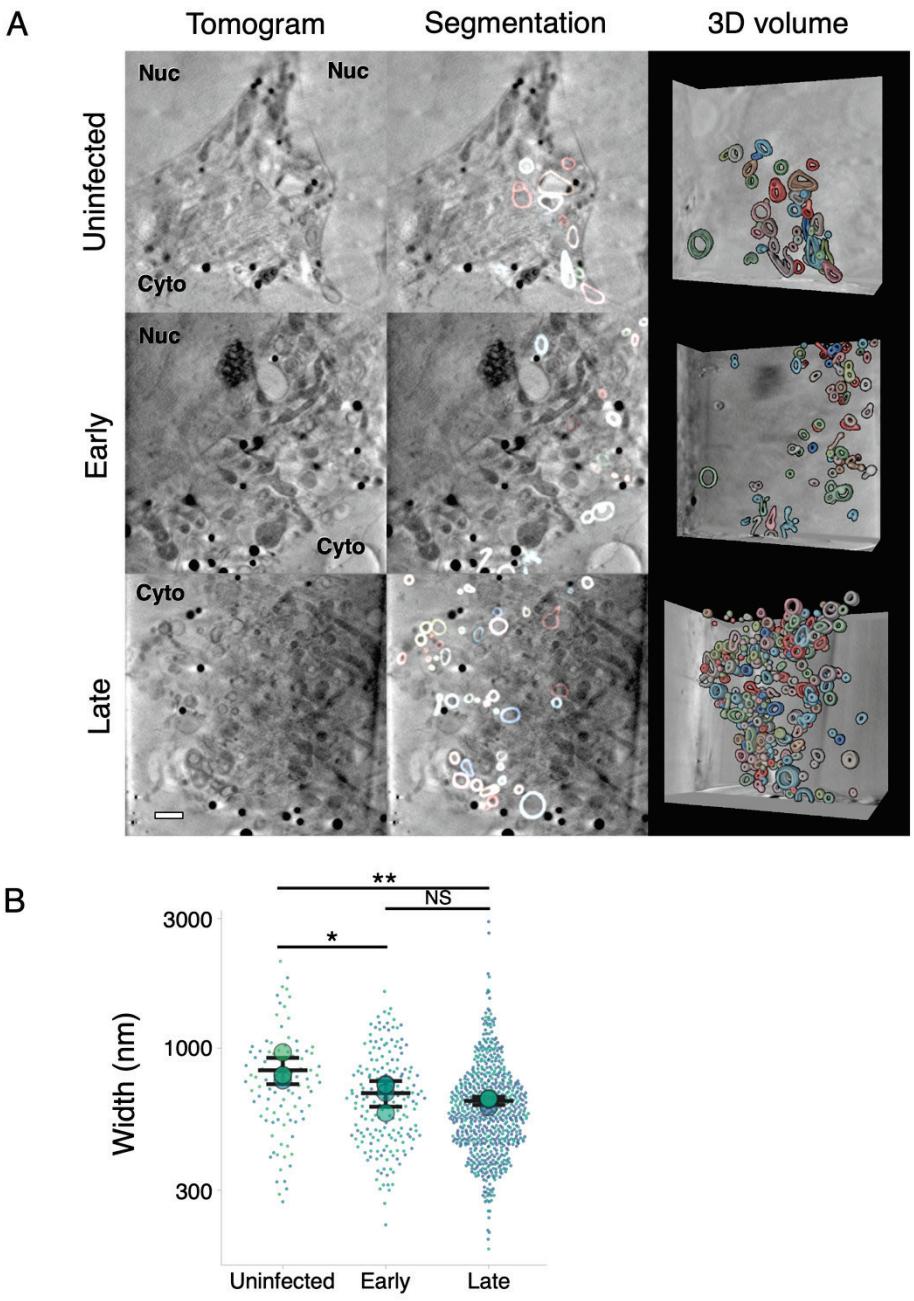

584

585 **Fig. 4. Remodelling of cytoplasmic vesicles during HSV-1 infection.** CryoSXT tomograms were
586 recorded of cells classified as uninfected, early-stage infection (stages 1+2) or late-stage infection
587 (stages 3+4) with timestamp HSV-1 based on fluorescent cryo-wide field microscopy. Data are
588 representative of three independent experiments. Scale bar = 1 µm. (**A**) A higher concentration of
589 vesicles is observed at the juxtanuclear compartment in cells at early- or late-stages of infection
590 compared with uninfected cells. (**B**) The maximum width of each vesicle in three-dimensions was
591 measured in *Contour* (manuscript in preparation). Vesicles with a spherical, ellipsoidal, or dumbbell
592 shape were included in the analysis but vesicles with a shape that didn't fall into these categories were

593 excluded. Intra-luminal vesicles and vesicles that were not individually resolved by the segmentation
594 were also excluded from the analysis. Significance of differences was assessed with a one-way ANOVA
595 and Tukey tests for the combinations: uninfected-early ($p=0.04$), uninfected-late ($p=0.01$), and early-
596 late ($p=0.62$). Big circles show the mean vesicle width per tomogram (4 tomograms per condition). Error
597 bars show overall mean ± SD.

598

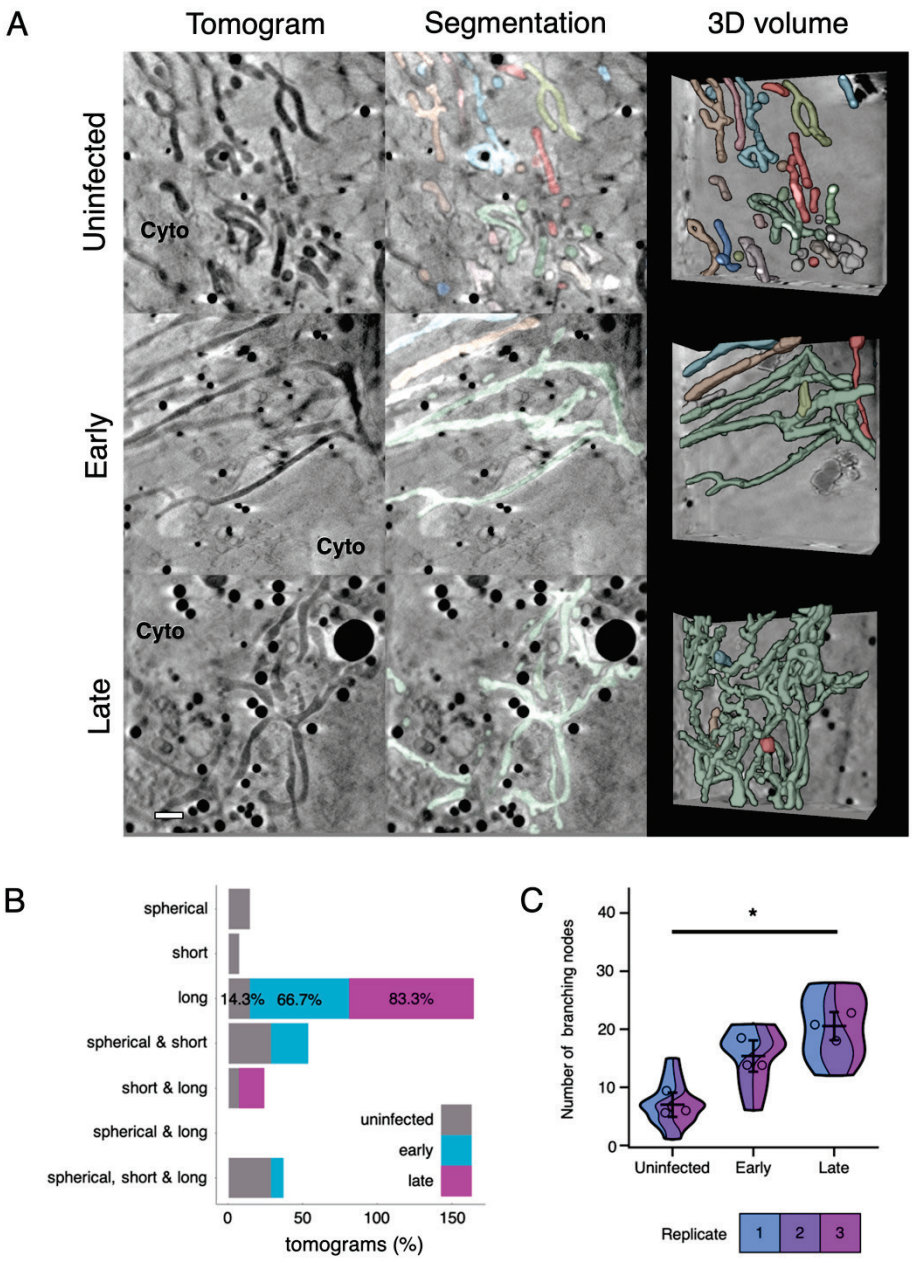

599

600 **Fig. 5. Remodelling of mitochondria during HSV-1 infection.** Morphological changes to
601 mitochondria were assessed from cryoSXT tomograms collected from uninfected cells and cells at
602 early- or late-stages of infection with timestamp HSV-1. Data are representative of three independent
603 experiments. Scale bars = 1 μm. (**A**) A shift towards elongated and branched mitochondria was
604 observed during infection. Mitochondria were segmented and differentiated using *Contour* to highlight
605 the abundance and 3D geometry of individual mitochondria. (**B**) The percentages of tomograms with
606 long mitochondria were greater for cells at early- or late-stages of infection than for uninfected cells in
607 replicate 2. Mitochondrial morphology was more heterogenous in uninfected cells. See **Supp. Fig 2** for

608 equivalent data from replicates 1 and 3. (**C**) The numbers of branching nodes were calculated for 45
609 tomograms across all replicates and significant differences in the number of nodes between uninfected
610 cells and those at late stages of infection were determined for each replicate using ANOVA and Tukey
611 tests ($p < 0.05$). Error bars show mean ± SD.

612

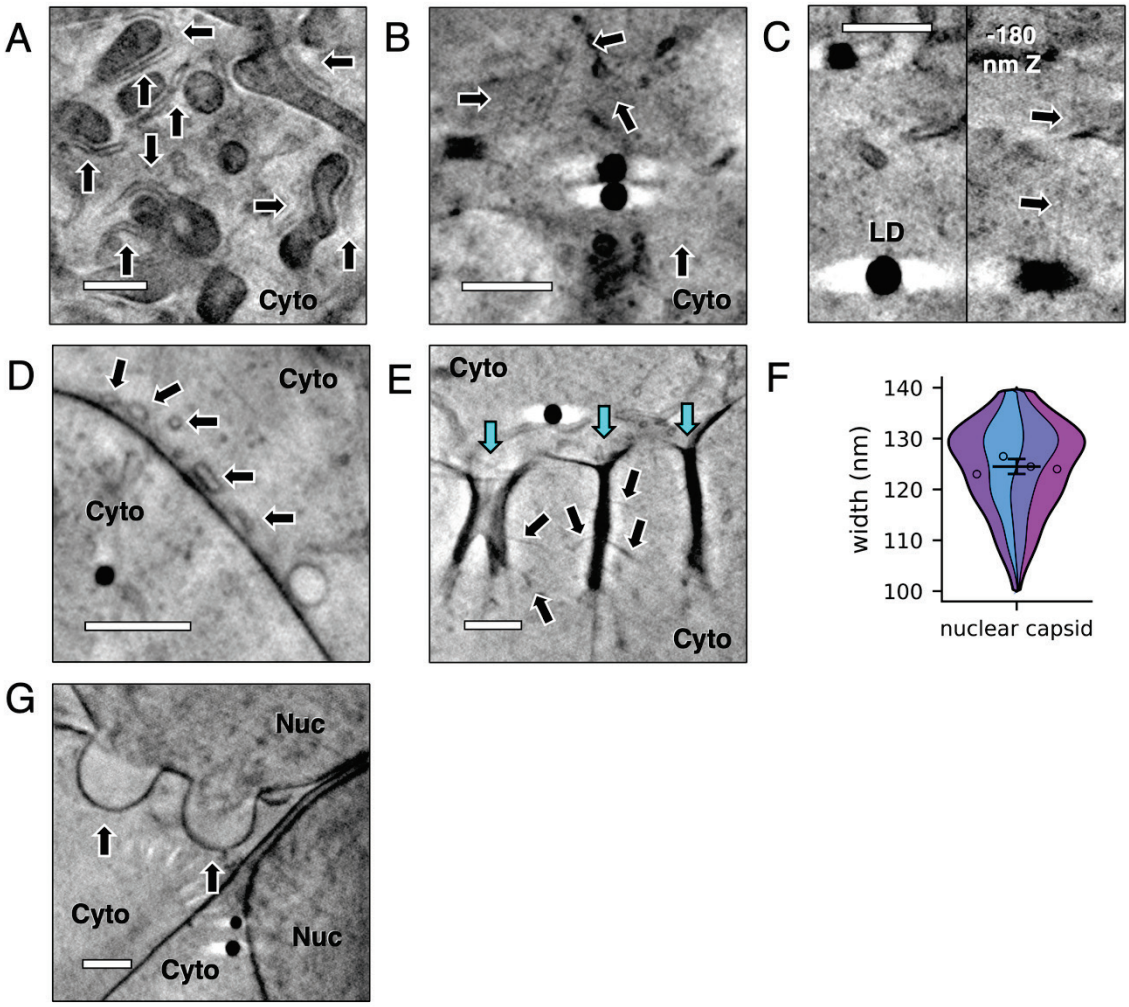

613

614 **Supp. Fig. 1. High resolution structures visible with the 25 nm zone plate objective**. 139 CryoSXT
615 tomograms were recorded from 107 cells using a 25 nm zone plate (ZP) objective and several structures
616 that were unrelated to HSV-1 infection were observed, including some that were not visible using the
617 40 nm zone plate objective. (**A**) The endoplasmic reticulum (ER) forms a silhouette (arrows) around the
618 mitochondria and the ER lumen is visible with the 25 nm zone plate. Cyto, cytoplasm. (**B**) Linear
619 structures resembling cytoskeletal filaments are visible with the 25 nm zone plate (arrows). (**C**) A
620 putative cytoskeletal filament (arrows) is in close apposition to a lipid droplet (LD) and may represent a
621 physical interaction. (**D**) Small vesicles with widths of 150–300 nm in the peripheral cytoplasm are
622 observed (arrows). (**E**) Large internalisations of the plasma membrane with depths of 1.6–2.2 µm (cyan)
623 and smaller side extensions (black arrows) are visible and may represent events of clathrin-independent
624 bulk endocytosis[77]. (**F**) The width of nuclear capsids was remeasured after imaging with the 25 nm zone
625 plate: 124.5 nm ± 0.96 nm SEM (n=80 from 4 tomograms; 8.55 nm SD). (**G**) Bulging of the nuclear
626 envelope is observed (arrows). We initially observed these in HSV-1 infection and thought it may

627 represent a virus-directed decrease in the integrity of the nuclear envelope, but we found multiple
628 examples in uninfected cells suggesting that they are a general feature of U2OS cells. Nuc, nucleus.

629

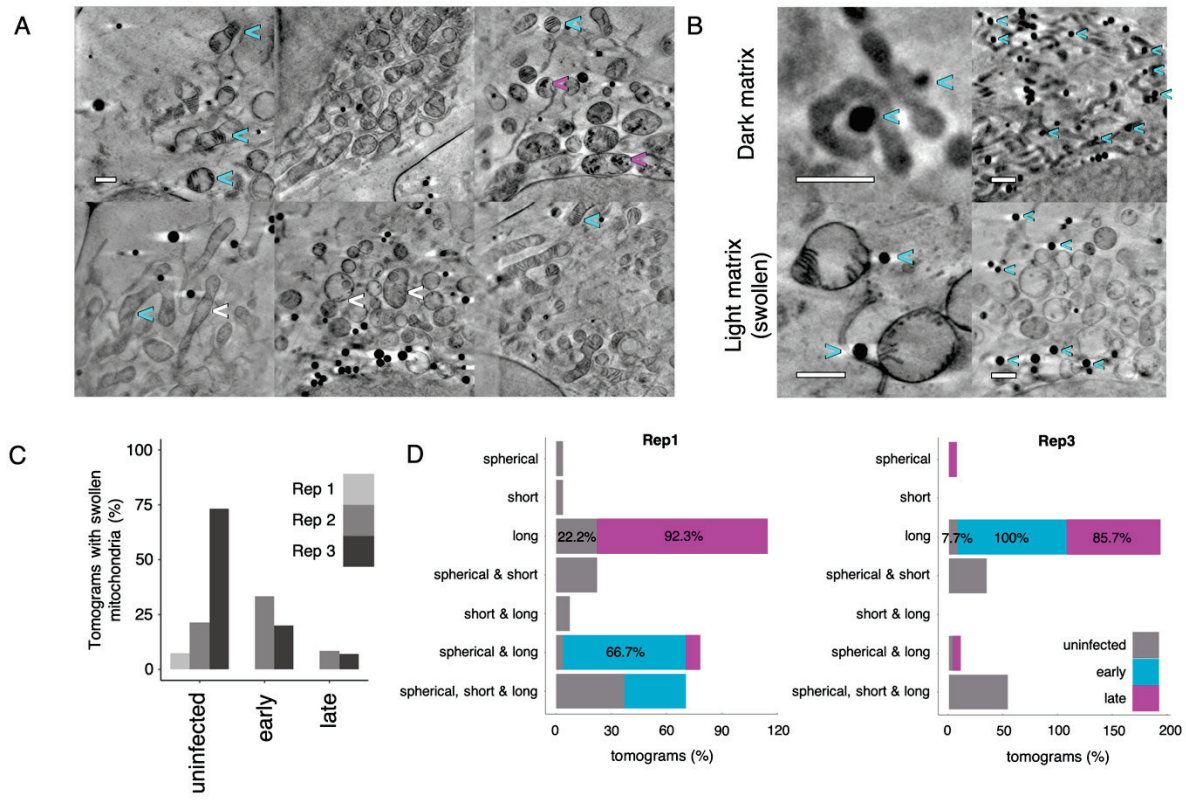

Supp. Fig. 2. The heterogenous morphology of mitochondria. Heterogenous mitochondrial morphologies are observed in cryoSXT tomograms collected from uninfected cells and cells at early and late stages of infection with timestamp HSV-1. Scale bars = 1 μm. (**A**) In some cases, mitochondria have light matrices with highly contrasting cristae (cyan arrows). This "swollen" phenotype has been reported to occur during cytochrome *c* release from porous mitochondria during apoptosis[44]. Dark matter is also observed in the matrix (magenta arrows) and may represent vesiculation. Small dark puncta are present in the matrix (white arrows) and could represent vesicles or short cristae. (**B**) Mitochondria with dark matrices were commonly coupled with lipid droplets (cyan arrows) but most lipid droplets were uncoupled from swollen mitochondria. (**C**) The percentages of tomograms with swollen mitochondria for uninfected cells and cells at early- or late-stages of infection in three independent replicates. (**D**) The percentages of tomograms collected from uninfected cells and those at early- or late-stages on infection in replicates 1 and 3 that contain different combinations of mitochondrial morphologies.

645 **Supp. Video 1. Segmentation of vesicles and mitochondria in the cytoplasm of a cell at a late**
646 **stage of infection.** CryoSXT data was collected from U2OS cells infected for 9 hours with 1 plaque-
647 forming unit per cell of the timestamp HSV-1 virus. Cryo-fluorescence microscopy revealed that this cell
648 was at a late stage of infection. The mitochondria were segmented using *Contour* and separate
649 mitochondria are colour-coded in shades of orange, red, pink and purple. Cytoplasmic vesicles were
650 segmented using *Segmentation Editor* in *ImageJ*. The vesicles were later differentiated and color-coded
651 using *Contour* and are displayed here in shades of blue and green. Field of view is 9.46×9.46 µm.

652 **Supp. Video 2. Segmentation of cytoplasmic vesicles reveals the effect of HSV-1 infection on**
653 **vesicle concentration at juxtanuclear sites.** CryoSXT data was collected from uninfected U2OS cells
654 and U2OS cells infected for 9 hours with 1 plaque-forming unit per cell of the timestamp HSV-1 virus.
655 Cytoplasmic vesicles were segmented using *Segmentation Editor* in *ImageJ*. The vesicles were later
656 differentiated and colour-coded using *Contour*. Fields of view are 9.46×9.46 µm.

657 **Supp. Video 3. Segmentation of mitochondria reveals the effect of HSV-1 infection on**
658 **mitochondrial morphology.** CryoSXT data was collected from uninfected U2OS cells and U2OS cells
659 infected for 9 hours with 1 plaque-forming unit per cell of the timestamp HSV-1 virus. Mitochondria were
660 segmented and colour-coded using *Contour* and appear elongated and branched in cells at late stages
661 of infection. Fields of view are 9.46×9.46 µm.

662

663 **References**

664 1. Nicoll, M. P., Proença, J. T. & Efstathiou, S. The molecular basis of herpes simplex virus latency.
665 *FEMS Microbiol. Rev.* **36**, 684–705 (2012).

666 2. Owen, D., Crump, C. & Graham, S. Tegument Assembly and Secondary Envelopment of
667 Alphaherpesviruses. *Viruses* **7**, 5084–5114 (2015).

668 3. Ahmad, I. & Wilson, D. W. HSV-1 Cytoplasmic Envelopment and Egress. *Int. J. Mol. Sci.* **21**, 5969
669 (2020).

670 4. Mettenleiter, T. C. Herpesvirus Assembly and Egress. *J. Virol.* **76**, 1537–1547 (2002).

671 5. Johnson, D. C. & Baines, J. D. Herpesviruses remodel host membranes for virus egress. *Nat. Rev.*
672 *Microbiol.* **9**, 382–394 (2011).

673 6. Crump, C. Virus Assembly and Egress of HSV. in *Human Herpesviruses* (eds. Kawaguchi, Y.,
674 Mori, Y. & Kimura, H.) 23–44 (Springer Singapore, 2018). doi:10.1007/978-981-10-7230-7_2.

675 7. Brown, J. C. & Newcomb, W. W. Herpesvirus capsid assembly: insights from structural analysis.
676 *Curr. Opin. Virol.* **1**, 142–149 (2011).

677 8. Bigalke, J. M. & Heldwein, E. E. Structural basis of membrane budding by the nuclear egress
678 complex of herpesviruses. *EMBO J.* **34**, 2921–2936 (2015).

679 9. Bigalke, J. M. & Heldwein, E. E. The Great (Nuclear) Escape: New Insights into the Role of the
680 Nuclear Egress Complex of Herpesviruses. *J. Virol.* **89**, 9150–9153 (2015).

681 10. Bigalke, J. M. & Heldwein, E. E. Nuclear Exodus: Herpesviruses Lead the Way. *Annu. Rev. Virol.*
682 **3**, 387–409 (2016).

683 11. Zeev-Ben-Mordehai, T. *et al.* Crystal Structure of the Herpesvirus Nuclear Egress Complex
684 Provides Insights into Inner Nuclear Membrane Remodeling. *Cell Rep.* **13**, 2645–2652 (2015).

685 12. Hernández Durán, A. *et al.* Protein interactions and consensus clustering analysis uncover insights
686 into herpesvirus virion structure and function relationships. *PLOS Biol.* **17**, e3000316 (2019).

687 13. Hollinshead, M. *et al.* Endocytic tubules regulated by Rab GTPases 5 and 11 are used for
688 envelopment of herpes simplex virus. *EMBO J.* **31**, 4204–4220 (2012).

689 14. Kotsakis, A., Pomeranz, L. E., Blouin, A. & Blaho, J. A. Microtubule Reorganization during Herpes
690 Simplex Virus Type 1 Infection Facilitates the Nuclear Localization of VP22, a Major Virion Tegument
691 Protein. *J. Virol.* **75**, 8697–8711 (2001).

15. Kim, J. A. *et al.* HSV-1 ICP27 induces apoptosis by promoting Bax translocation to mitochondria through interacting with 14-3-3θ. *BMB Rep.* **50**, 257–262 (2017).

16. Scherer, K. M. *et al.* A fluorescent reporter system enables spatiotemporal analysis of host cell modification during herpes simplex virus-1 replication. *J. Biol. Chem.* **296**, 100236 (2021).

17. Martin, C. *et al.* Herpes Simplex Virus Type 1 Neuronal Infection Perturbs Golgi Apparatus Integrity through Activation of Src Tyrosine Kinase and Dyn-2 GTPase. *Front. Cell. Infect. Microbiol.* **7**, 371 (2017).

18. Maeda, F. *et al.* Herpes Simplex Virus 1 UL34 Protein Regulates the Global Architecture of the Endoplasmic Reticulum in Infected Cells. *J. Virol.* **91**, (2017).

19. Ayache, J., Beaunier, L., Boumendil, J., Ehret, G. & Laub, D. Artifacts in Transmission Electron Microscopy. in *Sample Preparation Handbook for Transmission Electron Microscopy* 125–170 (Springer New York, 2010). doi:10.1007/978-0-387-98182-6_6.

20. Schnell, U., Dijk, F., Sjollema, K. A. & Giepmans, B. N. G. Immunolabeling artifacts and the need for live-cell imaging. *Nat. Methods* **9**, 152–158 (2012).

21. Büttner, M. *et al.* Challenges of Using Expansion Microscopy for Super-resolved Imaging of Cellular Organelles. *ChemBioChem* **22**, 686–693 (2021).

22. Harkiolaki, M. *et al.* Cryo-soft X-ray tomography: using soft X-rays to explore the ultrastructure of whole cells. *Emerg. Top. Life Sci.* **2**, 81–92 (2018).

23. Lewis, R. A. Medical phase contrast x-ray imaging: current status and future prospects. *Phys. Med. Biol.* **49**, 3573–3583 (2004).

24. Garman, E. F. Developments in X-ray Crystallographic Structure Determination of Biological Macromolecules. *Science* **343**, 1102–1108 (2014).

25. Kounatidis, I. *et al.* 3D Correlative Cryo-Structured Illumination Fluorescence and Soft X-ray Microscopy Elucidates Reovirus Intracellular Release Pathway. *Cell* **182**, 515-530.e17 (2020).

26. Okolo, C. A. *et al.* Sample preparation strategies for efficient correlation of 3D SIM and soft X-ray tomography data at cryogenic temperatures. *Nat. Protoc.* **16**, 2851–2885 (2021).

27. Pérez-Berná, A. J. *et al.* Structural Changes In Cells Imaged by Soft X-ray Cryo-Tomography During Hepatitis C Virus Infection. *ACS Nano* **10**, 6597–6611 (2016).

28. Laine, R. F. *et al.* Structural analysis of herpes simplex virus by optical super-resolution imaging. *Nat. Commun.* **6**, 5980 (2015).

722 29. Yuan, S. *et al.* Cryo-EM structure of a herpesvirus capsid at 3.1 Å. *Science* **360**, eaao7283 (2018).

723 30. von Hofsten, O. *et al.* Sub-25-nm laboratory x-ray microscopy using a compound Fresnel zone
724 plate. *Opt. Lett.* **34**, 2631 (2009).

725 31. Mastronarde, D. N. & Held, S. R. Automated tilt series alignment and tomographic reconstruction
726 in IMOD. *J. Struct. Biol.* **197**, 102–113 (2017).

727 32. Blondeau, C. *et al.* Tetherin Restricts Herpes Simplex Virus 1 and Is Antagonized by Glycoprotein
728 M. *J. Virol.* **87**, 13124–13133 (2013).

729 33. Zenner, H. L., Mauricio, R., Banting, G. & Crump, C. M. Herpes simplex virus 1 counteracts tetherin
730 restriction via its virion host shutoff activity. *J. Virol.* **87**, 13115–13123 (2013).

731 34. Johnson, D. C., Webb, M., Wisner, T. W. & Brunetti, C. Herpes Simplex Virus gE/gI Sorts Nascent
732 Virions to Epithelial Cell Junctions, Promoting Virus Spread. *J. Virol.* **75**, 821–833 (2001).

733 35. Vijayakrishnan, S., McElwee, M., Loney, C., Rixon, F. & Bhella, D. In situ structure of virus capsids
734 within cell nuclei by correlative light and cryo-electron tomography. *Sci. Rep.* **10**, 17596 (2020).

735 36. Grünewald, K. *et al.* Three-Dimensional Structure of Herpes Simplex Virus from Cryo-Electron
736 Tomography. *Science* **302**, 1396–1398 (2003).

737 37. Drayman, N., Patel, P., Vistain, L. & Tay, S. HSV-1 single-cell analysis reveals the activation of
738 anti-viral and developmental programs in distinct sub-populations. *eLife* **8**, e46339 (2019).

739 38. Simpson-Holley, M., Colgrove, R. C., Nalepa, G., Harper, J. W. & Knipe, D. M. Identification and
740 Functional Evaluation of Cellular and Viral Factors Involved in the Alteration of Nuclear Architecture
741 during Herpes Simplex Virus 1 Infection. *J. Virol.* **79**, 12840–12851 (2005).

742 39. Deng, Z. *et al.* HSV-1 Remodels Host Telomeres to Facilitate Viral Replication. *Cell Rep.* **9**, 2263–
743 2278 (2014).

744 40. Cai, W. & Schaffer, P. A. Herpes simplex virus type 1 ICP0 regulates expression of immediate-
745 early, early, and late genes in productively infected cells. *J. Virol.* **66**, 2904–2915 (1992).

746 41. Deschamps, T. & Kalamvoki, M. Impaired STING Pathway in Human Osteosarcoma U2OS Cells
747 Contributes to the Growth of ICP0-Null Mutant Herpes Simplex Virus. *J. Virol.* **91**, (2017).

748 42. Visalli, R. J. & Brandt, C. R. The HSV-1 UL45 18 kDa gene product is a true late protein and a
749 component of the virion. *Virus Res.* **29**, 167–178 (1993).

750 43. Loret, S., Guay, G. & Lippé, R. Comprehensive Characterization of Extracellular Herpes Simplex
751 Virus Type 1 Virions. *J. Virol.* **82**, 8605–8618 (2008).

752 44. Sun, M. G. *et al.* Correlated three-dimensional light and electron microscopy reveals transformation
753 of mitochondria during apoptosis. *Nat. Cell Biol.* **9**, 1057–1065 (2007).

754 45. Miyazono, Y. *et al.* Uncoupled mitochondria quickly shorten along their long axis to form indented
755 spheroids, instead of rings, in a fission-independent manner. *Sci. Rep.* **8**, 350 (2018).

756 46. Eustaquio, T. *et al.* Electron microscopy techniques employed to explore mitochondrial defects in
757 the developing rat brain following ketamine treatment. *Exp. Cell Res.* **373**, 164–170 (2018).

758 47. Bosch, M. *et al.* Mammalian lipid droplets are innate immune hubs integrating cell metabolism and
759 host defense. *Science* **370**, eaay8085 (2020).

760 48. Samrat, S. K., Ha, B. L., Zheng, Y. & Gu, H. Characterization of Elements Regulating the Nuclear-
761 to-Cytoplasmic Translocation of ICP0 in Late Herpes Simplex Virus 1 Infection. *J. Virol.* **92**, (2018).

762 49. Lopez, P., Van Sant, C. & Roizman, B. Requirements for the Nuclear-Cytoplasmic Translocation
763 of Infected-Cell Protein 0 of Herpes Simplex Virus 1. *J. Virol.* **75**, 3832–3840 (2001).

764 50. Lengyel, J., Strain, A. K., Perkins, K. D. & Rice, S. A. ICP27-dependent resistance of herpes
765 simplex virus type 1 to leptomycin B is associated with enhanced nuclear localization of ICP4 and
766 ICP0. *Virology* **352**, 368–379 (2006).

767 51. Cai, M. *et al.* Identification of the molecular determinants for nuclear import of PRV EP0. *Biol.*
768 *Chem.* **400**, 1385–1394 (2019).

769 52. Pasdeloup, D., Labetoulle, M. & Rixon, F. J. Differing Effects of Herpes Simplex Virus 1 and
770 Pseudorabies Virus Infections on Centrosomal Function. *J. Virol.* **87**, 7102–7112 (2013).

771 53. Avitabile, E. *et al.* Redistribution of microtubules and Golgi apparatus in herpes simplex virus-
772 infected cells and their role in viral exocytosis. *J. Virol.* **69**, 7472–7482 (1995).

773 54. Vyas, N. *et al.* Cryo-Structured Illumination Microscopic Data Collection from Cryogenically
774 Preserved Cells. *J. Vis. Exp.* 62274 (2021) doi:10.3791/62274.

775 55. Sukhorukov, V. M., Dikov, D., Reichert, A. S. & Meyer-Hermann, M. Emergence of the
776 Mitochondrial Reticulum from Fission and Fusion Dynamics. *PLoS Comput. Biol.* **8**, e1002745
777 (2012).

778 56. Youle, R. J. & van der Bliek, A. M. Mitochondrial Fission, Fusion, and Stress. *Science* **337**, 1062–
779 1065 (2012).

780 57. Bartolák-Suki, E., Imsirovic, J., Nishibori, Y., Krishnan, R. & Suki, B. Regulation of Mitochondrial
781 Structure and Dynamics by the Cytoskeleton and Mechanical Factors. *Int. J. Mol. Sci.* **18**, 1812
782 (2017).

783 58. Bowes, T. & Gupta, R. S. Novel mitochondrial extensions provide evidence for a link between
784 microtubule-directed movement and mitochondrial fission. *Biochem. Biophys. Res. Commun.* **376**,
785 40–45 (2008).

786 59. Silva Ramos, E., Larsson, N.-G. & Mourier, A. Bioenergetic roles of mitochondrial fusion. *Biochim.*
787 *Biophys. Acta BBA - Bioenerg.* **1857**, 1277–1283 (2016).

788 60. Liu, X. & Hajnóczky, G. Altered fusion dynamics underlie unique morphological changes in
789 mitochondria during hypoxia–reoxygenation stress. *Cell Death Differ.* **18**, 1561–1572 (2011).

790 61. Li, J. *et al.* Mitochondrial elongation-mediated glucose metabolism reprogramming is essential for
791 tumour cell survival during energy stress. *Oncogene* **36**, 4901–4912 (2017).

792 62. Combs, J. A. *et al.* Human Cytomegalovirus Alters Host Cell Mitochondrial Function during Acute
793 Infection. *J. Virol.* **94**, (2020).

794 63. Li, Y., Boehning, D. F., Qian, T., Popov, V. L. & Weinman, S. A. Hepatitis C virus core protein
795 increases mitochondrial ROS production by stimulation of Ca2+ uniporter activity. *FASEB J.* **21**,
796 2474–2485 (2007).

797 64. Muraro, S. P. *et al.* Respiratory Syncytial Virus induces the classical ROS-dependent NETosis
798 through PAD-4 and necroptosis pathways activation. *Sci. Rep.* **8**, 14166 (2018).

799 65. Lassoued, S. *et al.* Epstein-Barr virus induces an oxidative stress during the early stages of
800 infection in B lymphocytes, epithelial, and lymphoblastoid cell lines. *Mol. Cell. Biochem.* **313**, 179–
801 186 (2008).

802 66. Tanaka, M., Sata, T. & Kawaguchi, Y. The product of the Herpes simplex virus 1 UL7 gene interacts
803 with a mitochondrial protein, adenine nucleotide translocator 2. *Virol. J.* **5**, 125 (2008).

804 67. Derakhshan, M., Willcocks, M. M., Salako, M. A., Kass, G. E. N. & Carter, M. J. Human herpesvirus
805 1 protein US3 induces an inhibition of mitochondrial electron transport. *J. Gen. Virol.* **87**, 2155–2159
806 (2006).

807 68. Saffran, H. A., Pare, J. M., Corcoran, J. A., Weller, S. K. & Smiley, J. R. Herpes simplex virus
808 eliminates host mitochondrial DNA. *EMBO Rep.* **8**, 188–193 (2007).

809 69. Chadha, P. *et al.* Domain Interaction Studies of Herpes Simplex Virus 1 Tegument Protein UL16
810 Reveal Its Interaction with Mitochondria. *J. Virol.* **91**, e01995-16 (2017).

811 70. McSharry, B. P., Jones, C. J., Skinner, J. W., Kipling, D. & Wilkinson, G. W. G. Human telomerase
812 reverse transcriptase-immortalized MRC-5 and HCA2 human fibroblasts are fully permissive for
813 human cytomegalovirus. *J. Gen. Virol.* **82**, 855–863 (2001).

814 71. Albecka, A. *et al.* Dual Function of the pUL7-pUL51 Tegument Protein Complex in Herpes Simplex
815 Virus 1 Infection. *J. Virol.* **91**, (2017).

816 72. Schindelin, J. *et al.* Fiji: an open-source platform for biological-image analysis. *Nat. Methods* **9**,
817 676–682 (2012).

818 73. Kenny, M. & Schoen, I. Violin SuperPlots: visualizing replicate heterogeneity in large data sets.
819 *Mol. Biol. Cell* **32**, 1333–1334 (2021).

820 74. Gómez-Rubio, V. ggplot2 - Elegant Graphics for Data Analysis (2nd Edition). *J. Stat. Softw.* **77**,
821 (2017).

822 75. Racine, J. S. RStudio: A Platform-Independent IDE for R and Sweave: Software Review. *J. Appl.*
823 *Econom.* **27**, 167–172 (2012).

824 76. Lord, S. J., Velle, K. B., Mullins, R. D. & Fritz-Laylin, L. K. SuperPlots: Communicating
825 reproducibility and variability in cell biology. *J. Cell Biol.* **219**, e202001064 (2020).

826 77. Shafaq-Zadah, M., Dransart, E. & Johannes, L. Clathrin-independent endocytosis, retrograde
827 trafficking, and cell polarity. *Curr. Opin. Cell Biol.* **65**, 112–121 (2020).

828